Applied Physics A (2025) 131:1
https://doi.org/10.1007/s00339-024-08057-7

Applied Physics A
Materials Science & Processing

Strain, pressure and temperature effects on linear and nonlinear optical properties of InP/InAs$_{1-x}$P$_x$/InP quantum well heterostructures

A. B. Davlatov[1] · A. H. Hameed[2,3] · K. Feddi[4] · P. J. Baymatov[1] · B. T. Abdulazizov[1] · A. A. Abdukarimov[1] · A. G. Al-Shatravi[5] · A. H. Al-Khursan[2,5] · L. M. Pérez[6] · D. Laroze[7] · E. Feddi[8]

Received: 10 September 2024 / Accepted: 4 November 2024 / Published online: 3 December 2024

Abstract
Optimizing the parameters that control the InAsP/InP quantum well (QW) system is of utmost importance for this system to give the best yield. Beginning from QW energy levels and momentum matrix element calculation, this work studies linear, nonlinear absorption and refractive index change, second harmonic generation (SHG), and third-harmonic generation (THG) in InAsP/InP QWs. Parameters controlling the structure, like hydrostatic pressure, temperature, well width, and phosphor mole fraction, are studied. The results show that the difference between energy levels increases with increasing temperature or reducing pressure. These differences are essential in obtaining SHG and THG. Pressure is more effective than the temperature in changing energy differences while increasing phosphor reduces the energy difference. So, one can choose the adjusted parameter (pressure or composition) according to the change in energy required. The pressure reduces absorption while temperature increases it. Increasing phosphor mole fraction reduces absorption; at high mole fraction, the absorption is approximately constant. The total refractive index change (RIC) is reduced with pressure or increasing molarity, but the higher molarity increases RIC. Increasing phosphor mole fraction reduced SHG and vice versa to THG. Increasing temperature increases SHG, and blue shifts its peak. For the pressure, it reduces SHG and redshifts its peak. Pressure increases THG and redshifts its peak while the temperature blue shifts THG peak. The effect of the temperature on the peak of the THG depends on the pressure: the temperature reduces the peak at low pressure, while the temperature increases it at high pressure. The results show the importance of such a study because the optical properties do not have a single-parameter effect; it has an interference effect of many parameters to produce the result.

Keywords Quantum well · *InAsP/InP* · Hydrostatic pressure · Temperature · Linear absorption · Nonlinear absorption · Second harmonic generation · Third-harmonic generation

1 Introduction

The quantized structures, which have a high surface-to-volume ratio, are superior to bulk structures in different fields, such as electronics, optoelectronics, photonics, spintronics, and energy conversion. They can be detectors, capacitors, and sensors. In these nanostructures, tuning their properties is possible by optimizing many parameters; for example, shifting energy states can change their linear and nonlinear response [1].

✉ E. Feddi
e.feddi@um5r.ac.ma

1 Namangan State University, 161 Boburshox Street, Namangan 160107, Uzbekistan

2 Nasiriya Nanotechnology Research Laboratory (NNRL), College of Science, University of Thi- Qar, Nasiriya, Iraq

3 General Directorate of Education, Thi-Qar, Iraq

4 Renewable Energy and Advanced Materials Laboratory, International University of Rabat, Morocco, Rabat

5 Department of Physics, College of Science, University of Thi-Qar, Nasiriya, Iraq

6 Departamento de Ingeniería Industrial y de Sistemas, Universidad de Tarapacá, Casilla 7D, Arica, Chile

7 Instituto de Alta Investigación, Universidad de Tarapacá, Casilla 7D, Arica, Chile

8 School of Applied and Engineering Physics, Mohammed VI Polytechnic University, Lot 660, Hay Moulay Rachid, 43150, Morocco, Ben Guerir

Through the optimization of a system, a question arises about the combination of parameters controlling processes, for example, to obtain much hardness and significantly lower stress, thermal and chemical stability, and optoelectronic characteristics [2]. Many other hurdles confronted the commercial production of micro-and-nano-structures, like device quality change, tribology, wear rates, and adhesion [3–5].

It is shown that the optical properties of the quantum wells (QWs) can be blue-shifted (high energy) under hydrostatic pressure. Both red and blue shifting in optical absorption can result under the control of both the hydrostatic pressure and temperature [6]. The binding energy can be enhanced under strain [7]. Small relaxation times with high oscillator strength and allowed transition energies make QWs a good candidate for high nonlinear optical properties [8].

As the bulk crystals have very low nonlinearity, obtaining high nonlinearity is formidable due to the electronic device transition limit and the lack of material emitting at mid- and far-infrared wavelengths. Thus, nanostructures can offer the required nonlinearity with high value by intersubband transitions. The nonlinearity is essential in various applications, including mobile communications, wireless networks, security screening, radio astronomy, and high-resolution radar [9–11].

Due to their large band offset and weak surface recombination, InAsP/InP quantum structures are getting attention in the development of semiconductor lasers. Since their earlier bulk counterparts, these structures take a situation in semiconductor lasers to build lasers that emit at low-loss and minimum dispersion points of 1.3, $1.5\mu\, m$ telecommunication wavelengths. Phosphorous-indium compounds have less adsorption and sticking coefficient than phosphorous-arsenic ones and appear at a high arsenic ratio. This is because of the inherent strain in the InAsP when grown on InP substrates. Localized states are caused, and charge localization becomes obvious [12]. Also, the lattice mismatching between the InP-based structure and Si highly deletoriate their integration [13].

The nonlinear optical properties of quantized structures depend on the conduction intersubband transitions [7]. The intersubband transitions are essential in nonlinear properties due to their significant oscillator strength with a narrow bandwidth. These two conditions are critical in fundamental applications such as infrared nonlinear applications, all-optical switching, high-speed modulators, and photodetectors [14, 15]. The second harmonic generation (SHG) will require the asymmetry of the structure. This asymmetry occurs via applying an external electric field or modulation of doped structures where asymmetric shapes are attained. The latter possibility is underhand by nanostructure growth methods. This paves the way for the development of devices in different fields of application, such as high-speed modulators, far-infrared photodetectors, color-tunable sources, optical filters, and semiconductor optical amplifiers [9]. Reducing dimensions increases the quantum size effect, and the nonlinearity rises. The confinement potential can also offer an asymmetry for the SHG, while third-order nonlinear susceptibility depends on the intersubband transitions [14].

Ungan et al. show that the electric and magnetic fields shift both the peak and position of the SHG and nonlinear optical rectification of the semi-parabolic QW [15]. Dakhlaoui et al. shows the effect of pressure on GaAs QW. They also showed that the energy difference between levels and the confining potential causes this absorption change due to doping position and pressure [16]. Li et al. show that spatial change of the effective mass strongly affects optical absorption, third-harmonic generation (THG), and refractive index change on GaAs QW [17]. Hien studied the effect of electron temperature, hydrostatic pressure, and alloy composition on GaAs QWs, showing the impact of these parameters, especially at phonon absorption [18]. Karabulut et al. show that structure parameters and the hydrostatic pressure control the nonlinear optical properties in asymmetric QWs [19].

Many theories of elasticity are proposed for nanostructures. The classical kinematics of the elasticity model are considered parallel with the nonlocality of the gradient effects. The gradient theory of strain predicts, in an effective form, the stiff phenomenon at these nanoscales. The elasticity nonlocal theory covers interactions at a long range. Both elasticity theories of gradient strain and nonlocal one cannot predict the overall material spectrum of the nanostructure [20–23]. Faghidian and Tounsi provide a critical analysis of nanostructures. Their analysis combined the stress and strain gradient with the classical elasticity theory [24].

This work continues to discover the linear and nonlinear absorption coefficient and refractive index in InAsP/InP QWs. It begins by calculating their energy levels at different sizes and studying them under different mole fractions, QW sizes, pressure, and temperature. It is shown that pressure is more effective than temperature in changing the energy difference between QW levels, which is reduced with its increment. Absorption, refractive index change (RIC), and SHG are reduced with increasing phosphor mole fraction while THG increases. Temperature (Pressure) increases (reduces) SHG. The THG is increased with pressure. The

effect of the temperature on the THG peak depends on the applied pressure.

2 Theoretical frameworks

2.1 Electron energy level and wave function

Calculating the energy levels and wave functions in $InP/InAs_{1-x}P_x/InP$ quantum wells involves solving the Schrödinger equation for the confined charge carriers (electrons or holes) within the potential profile created by the layers of InP and $InAs_{1-x}P_x$. The effective mass approximation is for a bulk crystal, which means the crystal is so large concerning the scale of an electron wave function that it is effectively infinite. Within the effective mass approximation, the Schrodinger equation is as follows [25]:

$$-\frac{\hbar^2}{2}\frac{\partial}{\partial z}\frac{1}{m^*(z)}\frac{\partial}{\partial z}\psi(z)+V(z)\psi(z)=E\psi(z) \tag{1}$$

Here, $\hbar$ is the reduced Planck's constant, $m^*(z)$ is the effective mass of the charge carrier, $\psi(z)$ is the wave function, E is the energy of the particle. The potential energy profile $V(z)$ within the $InP/InAs_{1-x}P_x/InP$ quantum well is typically modelled as a step potential:

$$V(z)=\begin{cases}\Delta V_{CB}(x,P), & -\infty < z < 0\\ 0, & 0 < z < L\\ \Delta V_{CB}(x,P), & L < z < \infty\end{cases} \tag{2}$$

Here, L is the quantum well width (Fig. 1).

The pressure-dependent lattice constant is estimated using the following relation given by [26, 27]:

$$a_i(P)=a_i(0)\left[1+\left(\frac{B_i'}{B_i}\right)P\right]^{-1/(3B_i')} \tag{3}$$

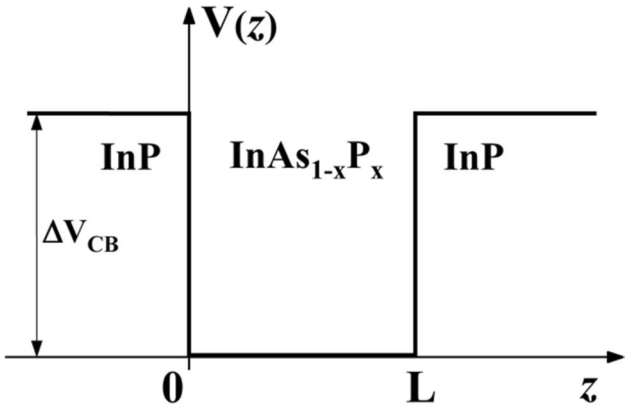

Fig. 1 Band diagram profile for $InP/InAs_{1-x}P_x/InP$ heterostructure (Finite deep potential well)

$i-$ refers to InP and $InAs_{1-x}P_x$. Here, B is the bulk modulus, and B' is the pressure derivative of the bulk modulus, $a(0)$ and $a(P)$ are the lattice parameters at pressures $P=0$ and $P\neq 0$, respectively. The modified band offsets confinement potentials for the conduction band (CB), taking into account the cumulative effects of the strain and hydrostatic pressure are given as [28, 28],

$$\Delta V_{CB}(x,P)=\Delta V_{CB}(x)+\Delta V_{CB}^{hy}(x,P) \tag{4}$$

The offsets at zero pressure are estimated using Bir-Pikus Hamiltonian [26, 28], and the hydrostatic component of band offsets is expressed as:

$$\Delta V_{CB}^{hy}(x,P)=\frac{2}{3}2a_C(x)\left(1-\frac{C_{11}(x)}{C_{12}(x)}\right)\left[\frac{a_{InP}(P)-a_{InAs_{1-x}P_x}(x,P)}{a_{InAs_{1-x}P_x}(x,P)}\right] \tag{5}$$

Here, $a_C(x)$ is the Deformation potential constant, $C_{11}(x)$, $C_{12}(x)$ are the respective elastic constants, $\Delta V_{CB}(x)=V_{CB}(InP)-V_{CB}\left(InAs_{1-x}P_x\right)$, - is the energy difference (band offsets) between the CB of InP and that of $InAs_{1-x}P_x$ in the absence of hydrostatic pressure.

The electron effective mass in the CBs of InP and $InAs_{1-x}P_x$ are as follows [25]:

$$m^*(z)=\begin{cases}m^*_{InP}(E,P,T)=m^*_{InP(0)}(P,T)\left(1+\alpha_{InP}(P,T)\left(E-\Delta V_{CB}(x,P)\right)\right), & -\infty < z < 0\\ m^*_{InAs_{1-x}P_x}(E,P,T)=m^*_{InAs_{1-x}P_x(0)}(P,T)\left(1+\alpha_{InAs_{1-x}P_x}(P,T)E\right), & 0 < z < L\\ m^*_{InP}(E,P,T)=m^*_{InP(0)}(P,T)\left(1+\alpha_{InP}(P,T)\left(E-\Delta V_{CB}(x,P)\right)\right), & L < z < \infty\end{cases} \tag{6}$$

$m^*_{InP(0)}(P,T)$, $m^*_{InAs_{1-x}P_x(0)}(P,T)$ are the effective masses of an electron at the bottom of the CB. $m^*_{InP}(E,P,T)$, $m^*_{InAs_{1-x}P_x}(E,P,T)$ are the effective mass of an electron as a function of energy and hydrostatic pressure. $\alpha_{InP}(P,T)$, $\alpha_{InAs_{1-x}P_x}(P,T)$ are the nonparabolic coefficients.

The linear dimensions of the sample changed very little under the influence of temperature, so that they can be ignored. But, $E_g(T)$–the band gap of the sample changes noticeably [30],

$$E_g(T) = E_g(T=0) - \frac{\alpha_V T^2}{\beta_V + T} \tag{7}$$

Here: $\alpha_V$and β_V are the Varshni constants, T is the temperature.

Under the influence of hydrostatic pressure, geometric dimensions $L_x(P)$, $L_y(P)$ [31], and bandgap $E_g(P)$ [26, 32] of the sample changes significantly,

$$E_g(P) = E_g(P=0) + aP \tag{8}$$

$$L(P) = L(P=0)\left(1 - \left(S_{11} + 2S_{12}\right)P\right) \tag{9}$$

$$\alpha_i(P,T) = \frac{1}{E_{g(i)}(P,T)}\left(1 - \frac{m^*_{i(0)}(P,T)}{m_0}\right)^2 \tag{12}$$

According to the condition of continuity, the wave functions $\psi(z)$ at the points $z = 0$ and $z = L$ must be equal. We introduce the BenDaniel-Duke boundary condition to control the effective mass installation at the barrier-well boundary [36, 37]. These conditions lead to a set of transcendental equations that determine the allowed energy levels [25]:

$$E = \frac{\hbar^2}{2m^*_{InAs_{1-x}P_x}(E,P,T)L(P)^2} \left(\pi n - 2\mathrm{Arcsin}\left(\sqrt{\frac{\frac{m^*_{InP}(E,P,T)}{m^*_{InAs_{1-x}P_x}(E,P,T)}E}{\left(\frac{m^*_{InP}(E,P,T)}{m^*_{InAs_{1-x}P_x}(E,P,T)} - 1\right)E + \Delta V_{CB}(x,P)}}\right)\right)^2 \tag{13}$$

The wave function takes the following form:

$$\psi(z) = \begin{cases} \frac{(2\chi\gamma)^{3/2}\beta e^{\chi z}}{\sqrt{\left|(\chi^2-\gamma^2\beta^2)\gamma^3\beta^2 sin^2(\gamma L)+(\gamma^4\beta^3\chi-2\gamma^2\beta^2\chi^3-2\chi^5)sin(2\gamma L)-4L\chi^3\gamma^3\beta^2+4\chi^5\gamma L-5\gamma^3\beta^2\chi^2\right|}}, & z<0 \\ \frac{(2\chi)^{3/2}\sqrt{\gamma}(\chi\, sin(\gamma z)+\gamma\beta\, cos(\gamma z))}{\sqrt{\left|(\chi^2-\gamma^2\beta^2)\gamma^3\beta^2 sin^2(\gamma L)+(\gamma^4\beta^3\chi-2\gamma^2\beta^2\chi^3-2\chi^5)sin(2\gamma L)-4L\chi^3\gamma^3\beta^2+4\chi^5\gamma L-5\gamma^3\beta^2\chi^2\right|}}, & 0<z<L \\ \frac{(2\gamma)^{3/2}\sqrt{\chi}\beta(\gamma\beta\, sin(\alpha L)-\chi\, cos(\gamma L))e^{\chi(L-z)}}{\sqrt{\left|(\chi^2-\gamma^2\beta^2)\gamma^3\beta^2 sin^2(\gamma L)+(\gamma^4\beta^3\chi-2\gamma^2\beta^2\chi^3-2\chi^5)sin(2\gamma L)-4L\chi^3\gamma^3\beta^2+4\chi^5\gamma L-5\gamma^3\beta^2\chi^2\right|}}, & z>L \end{cases} \tag{14}$$

Here P is the hydrostatic pressure, $L(P=0)$ is the geometric dimension of the sample when not affected by hydrostatic pressure, a is the hydrostatic pressure parameters, S_{11} and S_{12} are the elastic constants. If we consider Eqs. (7 and 8), then the bandgap $E_g(P,T)$ of the sample under the influence of hydrostatic pressure and temperature is expressed as follows [33]:

$$E_{g(i)}(p,T) = E_{g(i)}(0,0) + a_i p - \frac{\alpha_{V(i)}T^2}{\beta_{V(i)} + T} \tag{10}$$

The current carriers' effective mass will equal the following [33],

$$m^*_{i(0)}(P,T) = m_0\left(1 + 2F_i + \frac{E_{P(i)}\left(E_{g(i)}(p,T) + 2\Delta_{so(i)}/3\right)}{E_{g(i)}(p,T)\left(E_{g(i)}(p,T) + \Delta_{so(i)}\right)}\right)^{-1} \tag{11}$$

The index i denotes InP and $InAs_{1-x}P_x$. Here: E_g is the Energy bandgap, E_P is the optical matrix parameter, Δ_{so} is the Spin-orbit splitting energy, F is the Kane parameter, m_0 is the mass of the free electron.

The electron band will be highly nonparabolic in semiconductors with a narrow bandgap. We use the Nelson model [35] to express the nonparabolicity coefficient,

Here, $\beta = \frac{m^*_{InP}(E,P,T)}{m^*_{InAs_{1-x}P_x}(E,P,T)}$-Effective mass ratio, $\chi = \sqrt{\frac{2m^*_{InP}(E,P,T)}{\hbar^2}\left(\Delta V_{CB}(x,P) - E\right)}$, $\gamma = \sqrt{\frac{2m^*_{InAs_{1-x}P_x}(E,P,T)}{\hbar^2}E}$ -Notations for solving the Schrödinger equation (corresponding to the wave vector).

2.2 Optical absorption coefficient, refractive index changes, second and third-harmonic generation coefficients

The mathematical formulation for the linear ($\alpha^{(1)}$) and the third-order nonlinear photo-absorption coefficient ($\alpha^{(3)}$) is derived from the density matrix approach and perturbation theory. Thus, the expression for absorption coefficient is written as [38]

$$\alpha(\omega, I) = \alpha^{(1)}(\omega) + \alpha^{(3)}(\omega, I) \tag{15}$$

where,

Table 1 Physical parameters for InAs, InP and $InAs_{1-x}P_x$ semiconductors samples [26, 39, 40]

Symbol	Parameters	InAs	InP	$InAs_{1-x}P_x$
$E_g(eV)$	Bandgap energy	0.42	1.424	$0.42(1-x)+1.424x+(1-x)x$
$a_0(A^o)$	Lattice constant	6.0584	5.8688	6.0584 − 0.1896x
$\alpha_V(10^{-3}\times eV/K)$	Varshni constants	0.276	0.363	$0.276+0.087x$
$\beta_V(K)$	Varshni constants	93	162	$93+69x$
$a_c(eV)$	Deformation Potentials	−5.08	−5.04	$-5.08+0.04x$
$C_{11}(10^3\times kbar)$	Elastic constants	0.833	1.011	$0.833+0.178x$
$C_{12}(10^3\times kbar)$	Elastic constants	0.453	0.561	$0.453+0.108x$
$S_{11}(10^{-3}\times 1/kbar)$	Elastic constants	1.945	1.639	1.945 − 0.306x
$S_{12}(10^{-3}\times 1/kbar)$	Elastic constants	−0.685	−0.589	$-0.685+0.096x$
$B(kbar)$	Bulk modulus	579	723	$579+144x$
B'	Pressure derivative of the bulk modulus	4.79	4.59	4.79 − 0.2x
$a(10^{-3}\times eV/kbar)$	Hydrostatic pressure parameters	11.4	8.2	11.4 − 3.2x
$\Delta_{so}(eV)$	Spin-orbit splitting energy	0.38	0.108	0.38 − 0.272x
ϵ_r	Relative permittivity	15.15	12.5	15.15 − 2.652x
$E_p(eV)$	Optical matrix parameter	21.5	20.07	21.5 − 0.79x
F	Kane parameter	−2.9	−1.31	$-2.9+1.59x$
$V_C(eV)$	Conduction band energy	0.795	1.353	$0.795+0.558x$

$$\alpha^{(1)}(\omega)=\omega\sqrt{\frac{\mu}{\epsilon_0\epsilon}}\frac{e^2\hbar\Gamma_{fi}\left|M_{fi}\right|^2\sigma}{\left(E_{fi}-\hbar\omega\right)^2+\left(\hbar\Gamma_{fi}\right)^2} \tag{16}$$

and

$$\alpha^{(3)}(\omega,I)=-\omega\sqrt{\frac{\mu}{\epsilon_0\epsilon}}\left(\frac{I}{2\epsilon_0 nc}\right)\frac{4\sigma e^4\hbar\Gamma_{fi}\left|M_{fi}\right|^4}{\left[\left(E_{fi}-\hbar\omega\right)^2+\left(\hbar\Gamma_{fi}\right)^2\right]^2}\times\left[1-\frac{\left|M_{ff}-M_{ii}\right|^2}{4\left|M_{fi}\right|^2}\left\{\frac{3E_{fi}^2-4\hbar\omega E_{fi}+\hbar^2\left(\omega^2-\Gamma_{fi}^2\right)}{E_{fi}^2+\left(\hbar\Gamma_{fi}\right)^2}\right\}\right] \tag{17}$$

μ is the system permeability, ϵ_0 is the vacuum permittivity, ϵ_r is the relative permittivity, σ is the electron density in the system, Γ is the relaxation rate, ω is the angular frequency of incident light, c is the speed of light, $n_r=\sqrt{\epsilon_r}$ is the refractive index of the system, I is the optical intensity of the incident photon, $M_{fi}=\psi_f|z|\psi_i$ and $E_{fi}=E_f-E_i$ denote the dipole moment matrix element for z-polarized light and the transition energy between state ψ_f and state ψ_i.

The sum of linear and nonlinear third-order refractive index changes is given by [38]:

$$\frac{\Delta n(\omega)}{n_r}=\frac{\Delta n^{(1)}(\omega)}{n_r}+\frac{\Delta n^{(3)}(\omega)}{n_r} \tag{18}$$

where,

$$\frac{\Delta n^{(1)}(\omega)}{n_r}=\frac{1}{2\epsilon_0 n_r^2}\frac{\sigma\left|M_{fi}\right|^2\left(E_{fi}-\hbar\omega\right)}{\left(E_{fi}-\hbar\omega\right)^2+\left(\hbar\Gamma_{fi}\right)^2} \tag{19}$$

and

$$\frac{\Delta n^{(3)}(\omega,I)}{n_r}=-\frac{\mu cI\sigma\left|M_{fi}\right|^4}{\epsilon_0 n_r^3}\frac{\left(E_{fi}-\hbar\omega\right)}{\left[\left(E_{fi}-\hbar\omega\right)^2+\left(\hbar\Gamma_{fi}\right)^2\right]^2}\times\times\left[1-\frac{\left|M_{ff}-M_{ii}\right|^2}{4\left|M_{fi}\right|^2\left(E_{fi}^2+\left(\hbar\Gamma_{fi}\right)^2\right)}\left\{\left[E_{fi}\left(E_{fi}-\hbar\omega\right)-\left(\hbar\Gamma_{fi}\right)^2\right]-\left(\hbar\Gamma_{fi}\right)^2\frac{\left(2E_{fi}-\hbar\omega\right)}{\left(E_{fi}-\hbar\omega\right)}\right\}\right] \tag{20}$$

The mathematical formulation of different polarization contributions can be deduced using the compact density matrix method. In this study, we will ignore the nonresonant terms that make a nonsignificant contribution. This work will focus on the SHG and THG defined, respectively, as follows [38]:

$$\chi_{2\omega}^{(2)}=\frac{\sigma}{\epsilon_0}\frac{M_{12}M_{23}M_{31}}{\left(\hbar\omega-E_{21}-j\hbar\Gamma_{21}\right)\left(2\hbar\omega-E_{31}-j\hbar\Gamma_{31}\right)} \tag{21}$$

$$\chi_{3\omega}^{(3)}=\frac{\sigma}{\epsilon_0}\frac{M_{12}M_{23}M_{34}M_{41}}{\left(\hbar\omega-E_{21}-j\hbar\Gamma_{21}\right)\left(2\hbar\omega-E_{31}-j\hbar\Gamma_{31}\right)\left(3\hbar\omega-E_{41}-j\hbar\Gamma_{41}\right)}$$

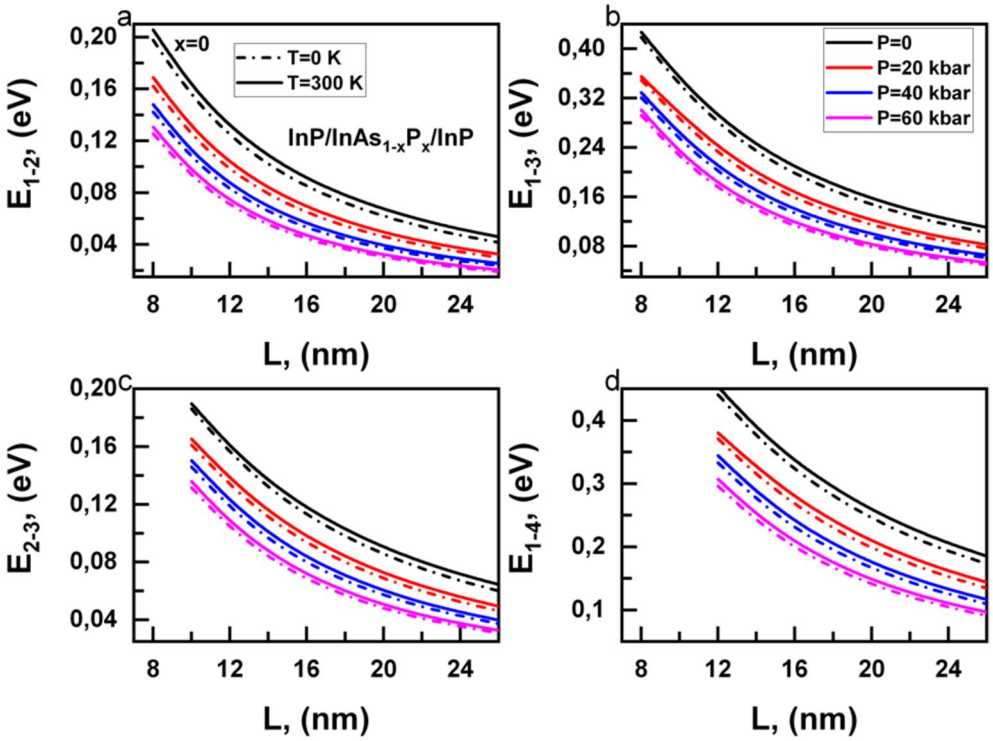

Fig. 2 Electron interlevel transition energies depend on the $InP/InAs_{1-x}P_x/InP$ quantum well size

3 Results and discussion

The used relations in this work are listed in Table 1. Additionally, the relaxation rate, the scattering cross-section, and the applied power used are $\Gamma = 3.5 \times 10^{12}\ s^{-1}$, $\sigma = 4 \times 10^{22}\ m^{-3}$, $I = 2 \times 10^{9}\ W/m^2$. Remember that $\mu = 4\pi \times 10^{-7}\ H/m, \epsilon_0 = 8.85 \times 10^{-12}\ F/m$.

Figure 2 shows the energy-level difference between states 1,2 (a), 1,3 (b), 2,3 (c), and 1,4 (d) versus the QW width at four values of hydrostatic pressure (0, 20, 40, 60 kbar) when the temperature is zero (dash-dotted curve) and 300 K (solid curve). The energy difference increases with increasing temperature or reducing pressure in all these figures. Pressure is more effective than temperature in changing energy differences. These differences are essential in obtaining $\chi^{(2)}$, $\chi^{(3)}$ as appears in the theory section. Note that M_{31} in symmetric systems is zero as M is an odd parameter, but it is not asymmetric systems like here. Hydrostatic pressure reduces the band offset for QW/barrier, causing more localized wavefunctions and localized energy states [16]. Such localization is more apparent in the lower energy states corresponding to higher ones, as shown when comparing E_{1-2} to E_{1-4} in Fig. 2a and d regarding their ordering. For example, in all graphs of Fig. 2, the energy difference between states with no pressure at $L = 16\ nm$ is equivalent to the case when $L = 26\ nm$ at $P = 60\ kbar$, i.e., 10 nm increment of QW width is to compensate the pressure effect.

Figure 3 studies the effect of phosphor mole fraction on the QW energy level difference at hydrostatic pressure $P = 20\ kbar$. It is shown that increasing phosphor reduces the energy difference, similar to increasing pressure in Fig. 2 above. This is also because phosphor increases the bandgap, see Table 1. Comparing Fig. 2a and 3a shows that at $L = 8\ nm$, the pressure reduces E_{1-2} by 0.04 eV while when $x = 0.2$, then E_{1-2} is reduced by 0.07 eV, i.e., phosphor reduces the energy difference more than pressure. So, one can choose the adjusted parameter according to the required change in energy.

Figure 4 shows the change in the momentum matrix element for the transitions between QW levels versus QW width at different pressures. It is shown that M_{1-3} is the smallest one. As we refer to in Fig. 2 above, such momentum is the lowest by the same polarity of the two energy states. In other figures (a, c, d), the momentum is increased with QW width and reduced with increasing pressure (or reduced temperature). As we refer to in Fig. 2, the momentum difference for respective states (1–2, 2–3) is more prominent than the irrespective ones (1–4 in d).

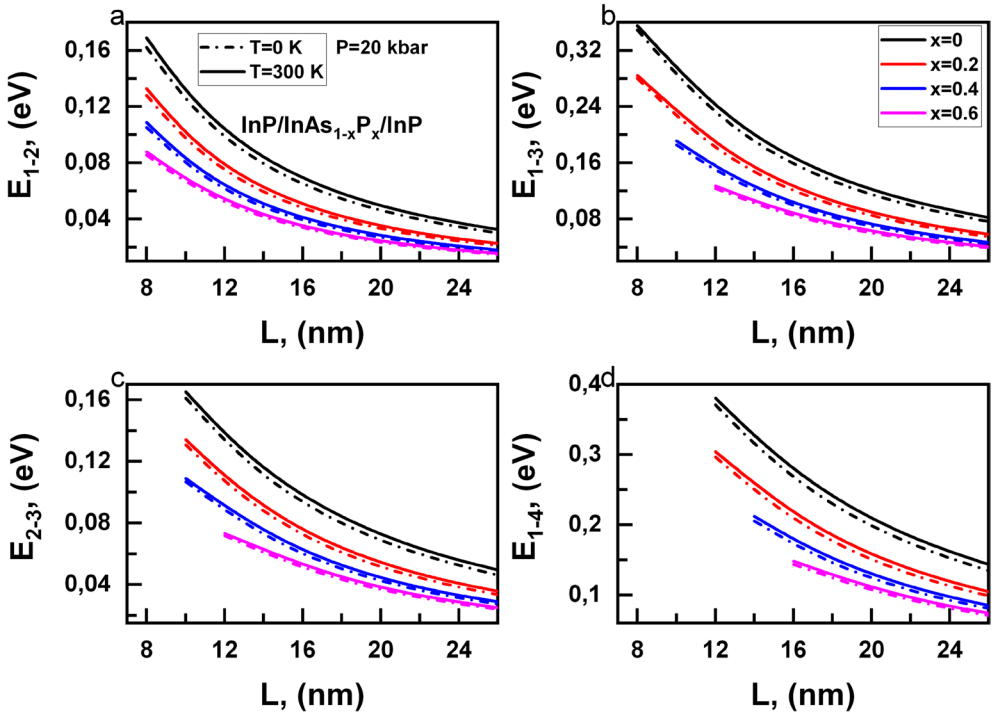

Fig. 3 Electron interlevel transition energies depend on the $InP/InAs_{1-x}P_x/InP$ quantum well size

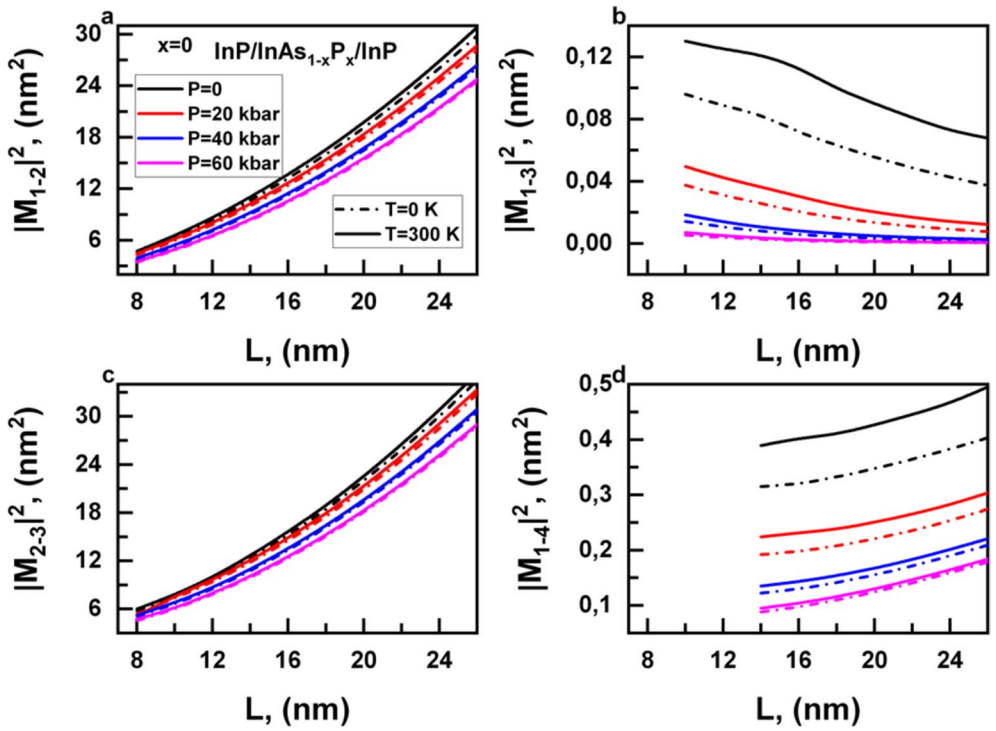

Fig. 4 Dependence of electron interlevel transition dipole moment matrix element on the size in $InP/InAs_{1-x}P_x/InP$ quantum well

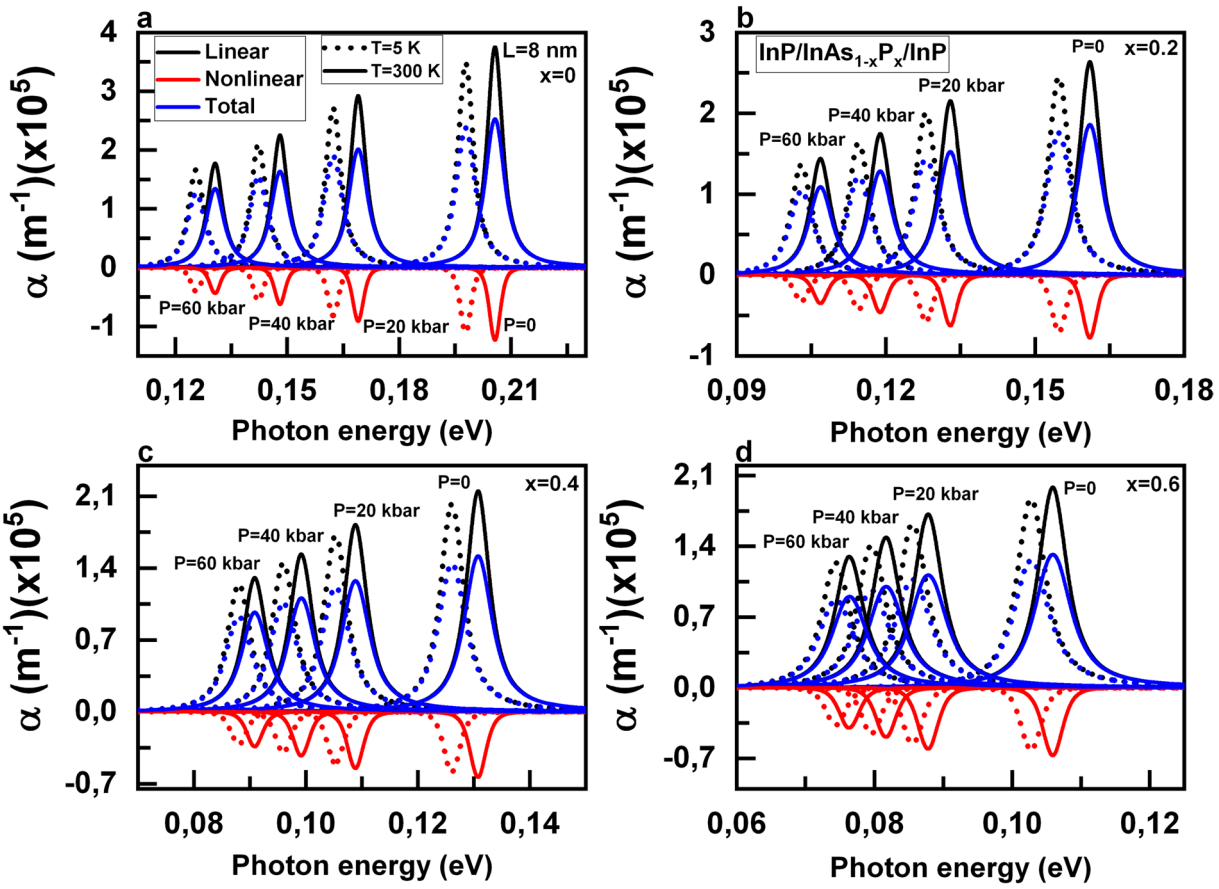

Fig. 5 Absorption coefficient as a function of the photon energy for InP/$InAs_{1-x}P_x$/InP quantum well

Figure 5 shows the linear, nonlinear, and total absorption coefficient versus photon energy at two temperatures and different pressures. The pressure reduces absorption while temperature increases it. Increasing phosphor mole fraction reduces absorption; at high mole fraction, the absorption is approximately constant. This can be ascribed to a few energy differences in Fig. 3 between energy levels of higher mole fractions. The results are in the range obtained by the literature [41]. The absorption reduction with pressure is a common conclusion due to changing QW parameters, such as the width and height of the confining potential, in addition to effective mass under pressure [19, 41].

Figure 6 is similar to Fig. 5, only here the QW width is increased to $L = 10\,nm$. While there is a prominent increment in absorption at zero phosphor, increasing molarity does not change the absorption. This is also discussed depending on Fig. 3, where the energy difference between QW levels is reduced with increasing well width, and the difference diminishes at longer widths. This is also the case of Fig. 7. Comparing Figs. 5, 6 and 7 shows that the absorption (linear, nonlinear, total) increases with increasing well width from $L = 8\,nm$ (in Fig. 5) to $L = 10\,nm$ (in Fig. 6), then somewhat reduction when $L = 12\,nm$ (Fig. 7). Such result works where the overall specified and geometrical parameters are controlling [42, 43]. For obvious comparison, Fig. 8 compares linear, nonlinear, and total absorption

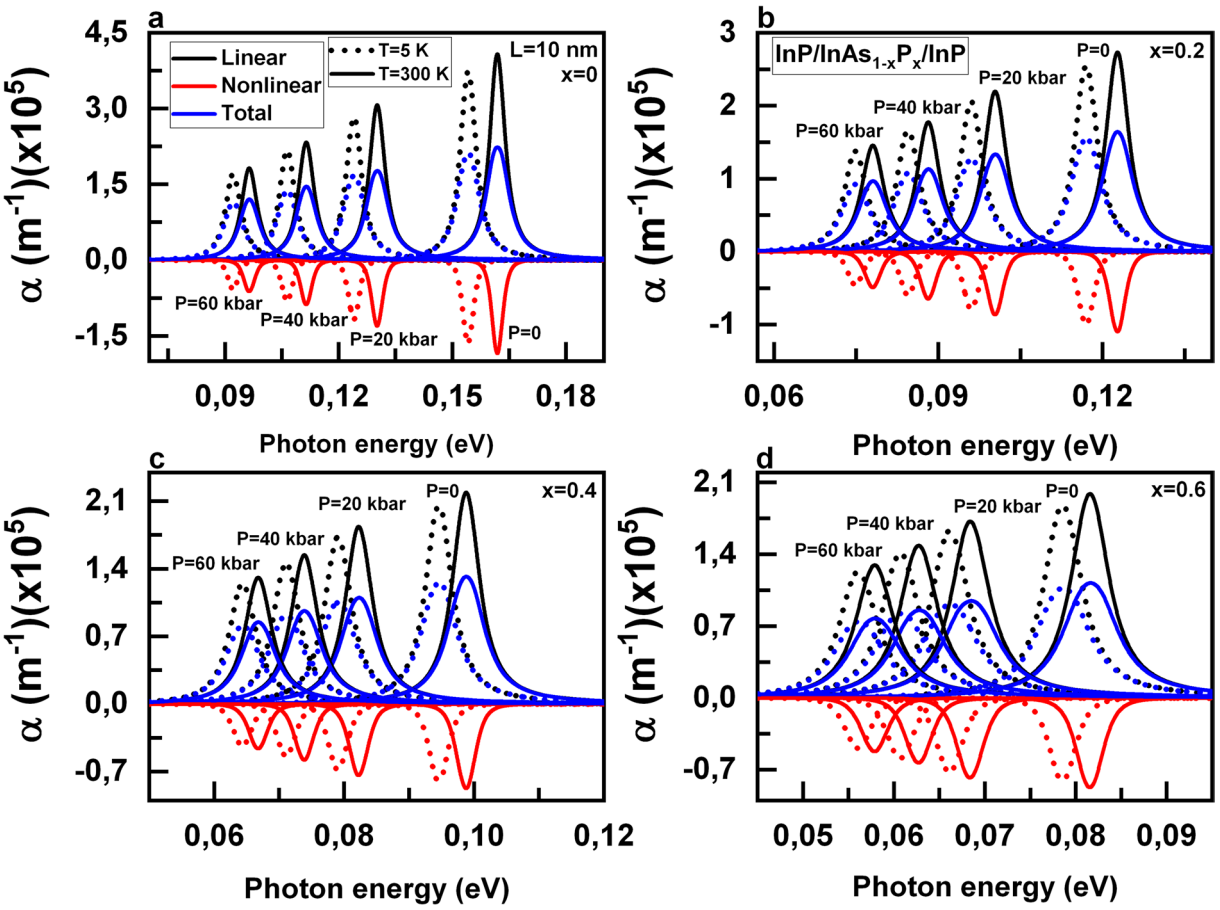

Fig. 6 Absorption coefficient as a function of the photon energy for InP/$InAs_{1-x}P_x$/InP quantum well

coefficients at different well widths. It can be ascribed to the momenta difference, see Fig. 4.

Figure 9 shows the linear, nonlinear, and total refractive index change (RIC) at two temperatures, hydrostatic pressure and mole fractions. The RIC is reduced with pressure and increasing molarity, but the higher molarity somewhat increases it. This figure shows the importance of such a study because the optical properties do not have a single-parameter effect; it has an interference effect of many parameters to produce the result. Figures 10 and 11 are also for RIC but at other values of QW width. It is shown that RIC is increased at these wider widths. Figure 12 abstracts these results where the increment in RIC is noticeable with well width.

Figure 13 shows the SHG of where the phosphor mole fraction reduced it, and blue shifts the peaks to higher energy. For example, the results are in the range of those in the literature [44]. Figure 14 shows that for THG, the behavior is inverse to the SHG, where the peak increases at a higher mole fraction and redshifts. Zhang and Yuan [43] also show a reduction in THG with increasing mole fraction in AlGaAs/GaAs QWs, but the values here are higher by three orders.

Figure 15 shows the SHG and THG of different temperatures and pressures. Increasing temperature increases SHG, and blue shifts it to higher energy. For the pressure, it reduces SHG and redshifts it to lower energy. For the THG,

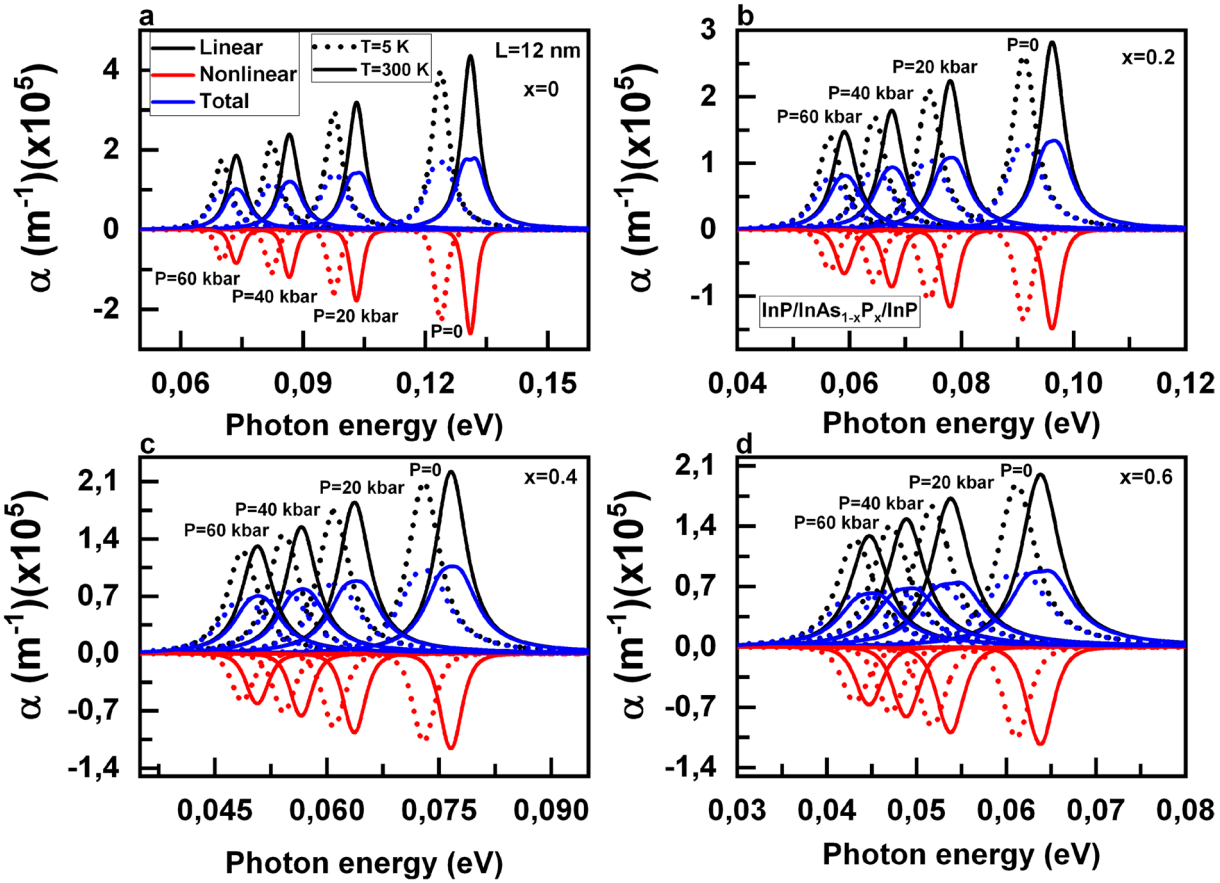

Fig. 7 Absorption coefficient as a function of the photon energy for InP/$InAs_{1-x}P_x$/InP quantum well

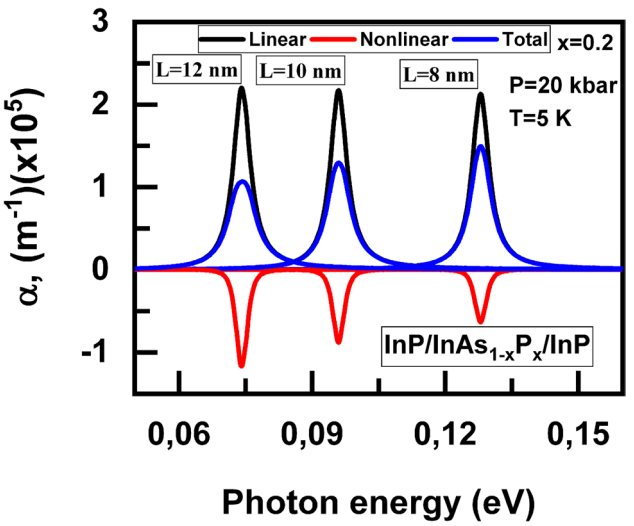

Fig. 8 Absorption coefficient as a function of the photon energy for InP/$InAs_{1-x}P_x$/InP quantum well

the temperature blue shifts the peak to higher energy, but the peak value varies with the applied pressure. At low pressure, the temperature reduces the peak; at high pressure, the temperature increases the peak. Equations (20) and (21) can view such variation, where the relation of THG depends on four momentum matrix elements while SHG depends on three. Each momentum depends on the wave functions of the QW energy levels related to the transition where the effective mass is introduced in the wave function relation (Eq. 14).

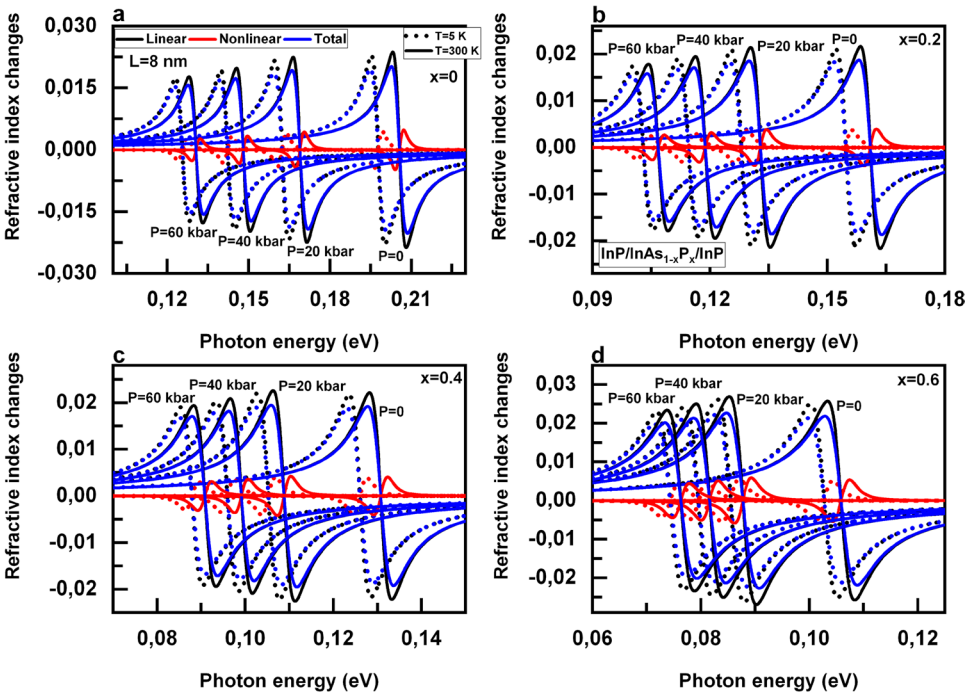

Fig. 9 Refractive index changes as a function of the photon energy for InP/$InAs_{1-x}P_x$/InP quantum well

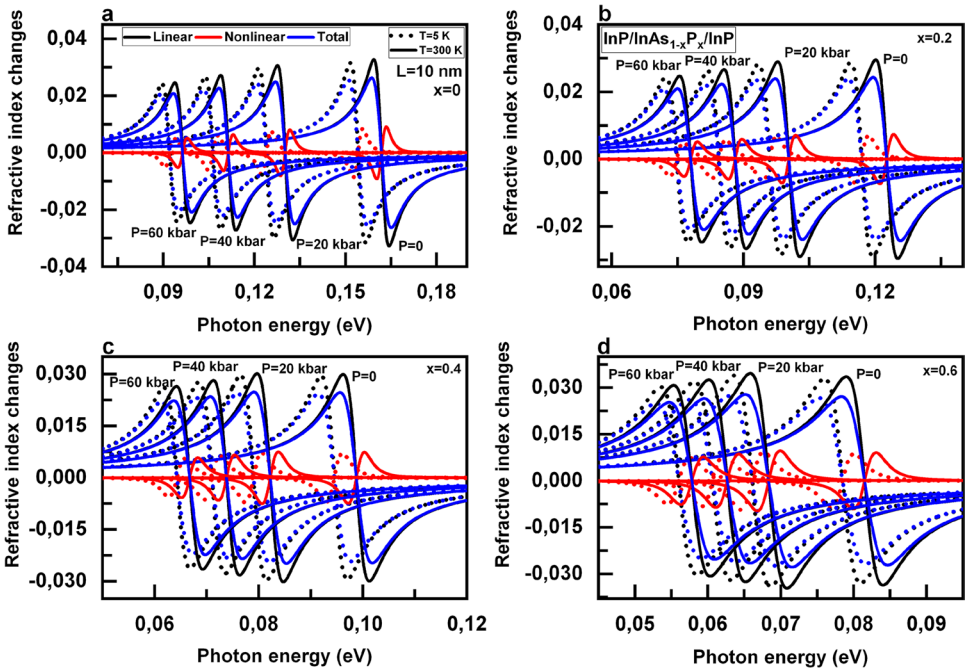

Fig. 10 Refractive index changes as a function of the photon energy for InP/$InAs_{1-x}P_x$/InP quantum well

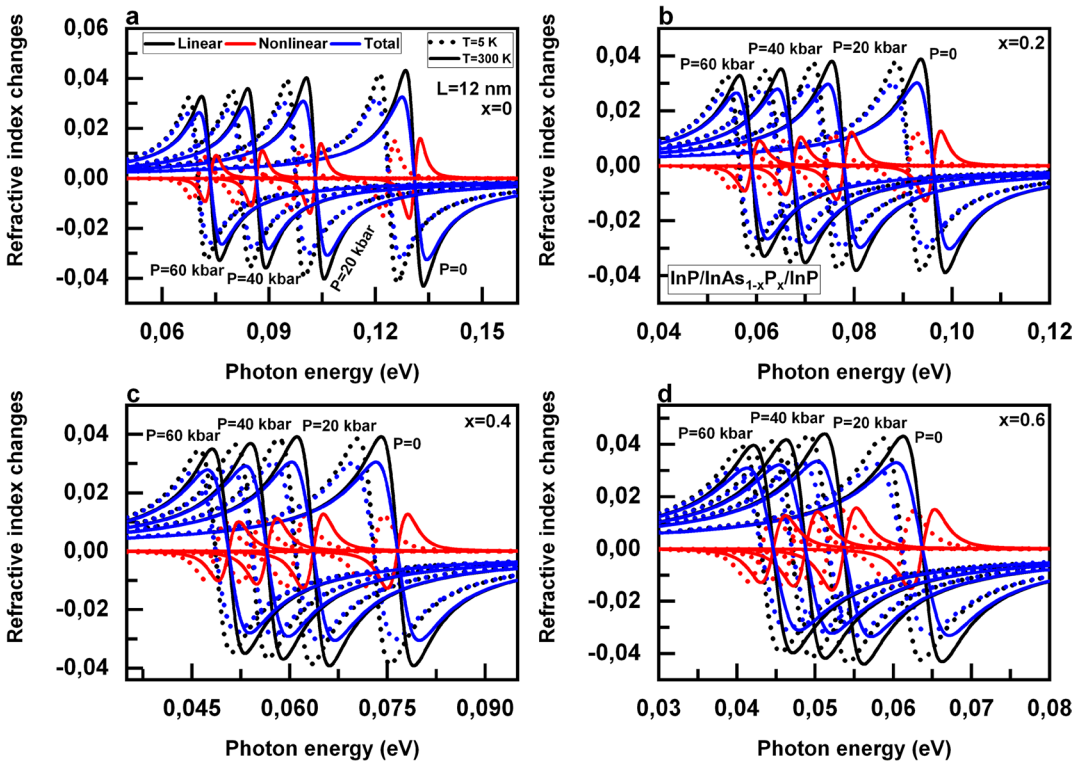

Fig. 11 Refractive index changes as a function of the photon energy for InP/$InAs_{1-x}P_x$/InP quantum well

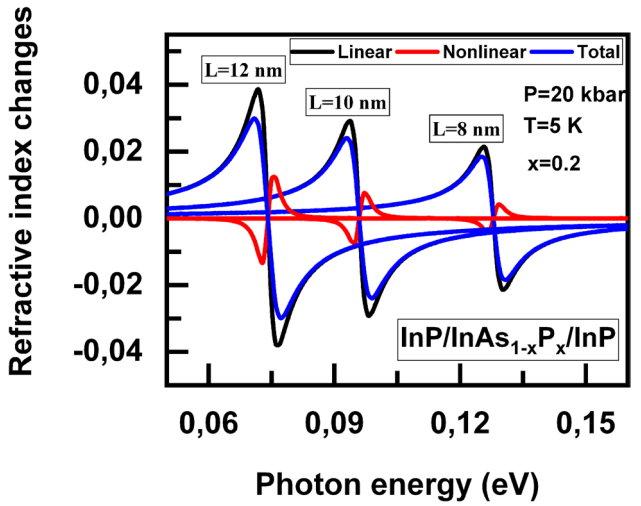

Fig. 12 Refractive index changes as a function of the photon energy for InP/$InAs_{1-x}P_x$/InP quantum well

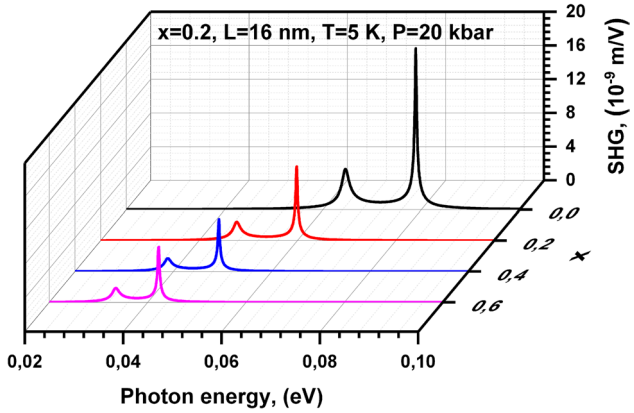

Fig. 13 Second-harmonic generation as a function of the photon energy for InP/$InAs_{1-x}P_x$/InP quantum well. L = 16 nm

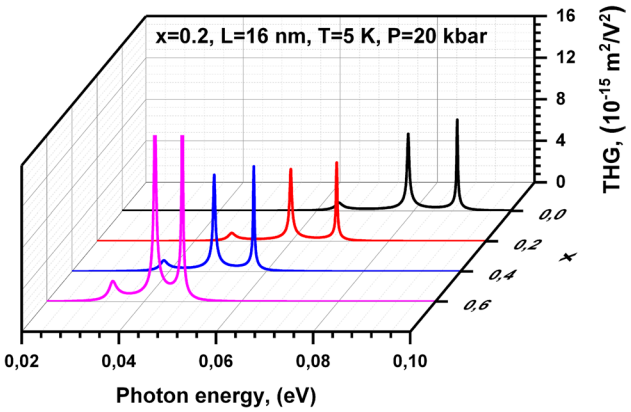

Fig. 14 Third harmonic generation as a function of the photon energy for $InP/InAs_{1-x}P_x/InP$ quantum well. L = 16 nm

4 Conclusion

Linear and nonlinear absorption and refractive index change, SHG, and THG in InAsP/InP QWs are studied in this work. The study covers the effect of hydrostatic pressure, temperature, well width, and phosphor mole fraction. The pressure and phosphor mole fraction reduces absorption and RIC while temperature increases them. Increasing phosphor mole fraction reduced SHG and vice versa to THG. Increasing temperature increases SHG, and blue shifts its peak. For the pressure, it reduces SHG and redshifts it. For the THG, pressure increases it. The effect of the temperature on the peak value of the THG depends on the pressure: the temperature reduces (increases) the peak at low (high) pressure. The results show the importance of such a study because the optical properties do not have a single-parameter effect; it has an interference effect of many parameters to produce the result.

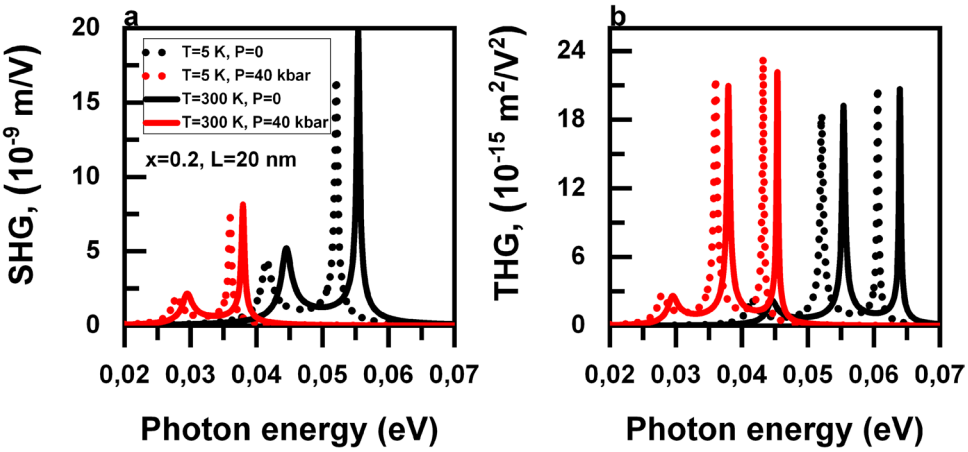

Fig. 15 Second-and Third harmonic generation as a function of the photon energy for InP/$InAs_{1-x}P_x$/InP quantum well. L = 20 nm

Acknowledgements This work was performed based on the Fundamental Research Grant Program FZ-20200929243 "The Effect of Hot Electrons and Phonons in a Strong Electromagnetic Field on the Characteristics of Semiconductor Solar Photovoltaic Elements and Nanostructures". LMP acknowledges financial support from ANID through *Convocatoria Nacional Subvención a Instalación en la Academia Convocatoria* Año 2021, Grant SA77210040. LMP and DL acknowledge partial financial support from ANID through FONDECYT 1240985.

Author contributions A.B. Davlatov: Conceptualization, methodology, software, writing—original draft preparation; A.H. Hameed : Investigation, resources, data curation; K. Feddi: validation, review, and editing; P.J. Baymatov: Formal analysis, visualization, and writing—review & editing ; B.T. Abdulazizov: Methodology, validation; A. Abdukarimov: Methodology, validation; A.G. Al-Shatravi: Investigation, resources; A.H. Al-Khursan: Writing—review & editing, validation; L.M. Pérez: Data curation, review & editing; D. Laroze: Supervision, validation, project administration; E. Feddi: Supervision, conceptualization, methodology, writing—review & editing.

Data availability The data supporting the findings of this study are available from the corresponding author upon reasonable request.

Declarations

Conflict of interest The authors declare that there is no conflict of interest regarding the publication of this manuscript.

References

1. J.E. Hamdaoui, L.M. Pérez, M.O. Martínez, N.E. Ouarie, P. Díaz, D. Laroze, E. Feddi, First Principle Study on the Effect of strain on the electronic structure and carrier mobility of the Janus MoSTe and WSTe Monolayers. Nanomaterials. **13**, 2535 (2023)
2. S. Neuville, Selective Carbon Material Engineering for Improved MEMS and NEMS. Micromachines. **10**, 539 (2019)
3. S. Neuville, Superconductivity described with Electron-Phonon Synchronic Coupling. Materials Today: Proceedings 5, 13827–13836 (2018)
4. S. Neuville, Quantum electronic mechanisms of atomic rearrangements during growth of hard carbon films. Surf. Coat. Technol. **206**, 703–726 (2011)
5. S. Neuville, Carbon Structure Analysis With Differentiated Raman Spectroscopy, : Refined Raman Spectroscopy Fundamentals For Improved Carbon Material Engineering. LAMBERT ACADEMIC PRESS, (2014), ISBN: 978-3-659-48909-9
6. A. El Aouami, M. Bikerouin, K. Feddi, N. Aghoutane, M. El-Yadri, E. Feddi, F. Dujardin, A. Radu, R.L. Restrepo, J.A. Vinasco, A.L. Morales, C.A. Duque, M.E. MoraRamos, Linear and nonlinear optical properties of a single dopant in GaN conical quantum dot with spherical cap. Phil. Mag. (2020). https://doi.org/10.1080/14786435.2020.1766711
7. M. El Haouari, A. Talbi, E. Feddi, H. El Ghazi, A. Oukerroum, F. Dujardin, Linear and nonlinear optical properties of a single dopant in strained AlAs/GaAs spherical core/shell quantum dots. Opt. Commun. **383**, 231–237 (2017)
8. J.C.M. Orozco, M.E. Mora-Ramos, C.A. Duque, Nonlinear optical rectification and second and third harmonic generation in GaAs d-FET systems under hydrostatic pressure. J. Luminescence. **132**, 449–456 (2012)
9. M. Abdullah, F.T.M. Noori, A.H. Al-Khursan, Terahertz emission in ladder plus Y-configurations in double quantum dot structure. Appl. Opt. **54**, 5168–5192 (2015)
10. H.H. AlAmeri, M. Abdullah, A.H. Al-Khursan, Second-harmonic generation of ultrashort pulses in refractive index linearly modulating quantum dot structure. Results Opt. **16**, 100706 (2024)
11. M. Abdullah, F.T.M. Noori, A.H. Al-Khursan, Terahertz emission in quantum dots by sum frequency generation. Curr. Appl. Phys. **16**, 763–771 (2016)
12. G. Vashisht, V.K. Dixit, S. Porwal, R. Kumar, T.K. Sharma, S.M. Oak, Charge carrier localization effects on the quantum efficiency and operating temperature range of InAsxP12x/InP quantum well detectors. J. Appl. Phys. **119**, 095708 (2016)
13. S.S. Hussein, A.G. Al-shatravi, A.H. Al-Khursan, Optical absorption from boron-containing quantum dot structures. Micro Nanostruct. **170**, 207375 (2022)
14. S. Sakiroglu, F. Ungan, U. Yesilgul, M.E.M. Ramos, C.A. Duque, E. Kasapoglu, H. Sari, I. Sökmen, Nonlinear optical rectification and the second and third harmonic generation in Pöschl–Teller quantum well under the intense laser field. Phys. Lett. A **376**, 1875–1880 (2012)
15. F. Ungan, J.C.M. Orozco, R.L. Restrepo, M.E.M. Ramos, E. Kasapoglu, C.A. Duque, Nonlinear optical rectification and second-harmonic generation in a semi-parabolic quantum well under intense laser field: effects of electric and magnetic fields. Superlattices Microstruct. **81**, 26–33 (2015)
16. H. Dakhlaoui, S. Almansour, E. Algrafy, Effect of Si d-doped layer position on optical absorption in GaAs quantum well under hydrostatic pressure. Superlattices Microstruct. **77**, 196–208 (2015)
17. K. Li, K. Guo, X. Jiang, M. Hu, Effect of position-dependent effective mass on nonlinear optical properties in a quantum well. Optik. **132**, 375–381 (2017)
18. N. D. Hien, Absorption and emission of longitudinal optical phonons by confined electrons in Pöschl–Teller quantum wells under the effects of the aluminum concentration, temperature, and hydrostatic pressure. J. Phys. Chem. Solids **179**, 111373 (2023)
19. I. Karabulut, U. Atav, H. Safak, M. Tomak, Second harmonic generation in an asymmetric rectangular quantum well under hydrostatic pressure. Phys. B **393**, 133–138 (2007)
20. S.A. Faghidian, I. Elishakof, The tale of shear coefficients in Timoshenko–Ehrenfest Beam theory: 130 years of progress. Meccanica. **58**, 97–108 (2023)
21. R. Barretta, S.A. Faghidian, F.M. de Sciarra, A consistent variational formulation of Bishop nonlocal rods. Continuum Mech. Thermodyn. **32**, 1311–1323 (2020)
22. S.A. Faghidian, Analytical approach for inverse reconstruction of eigenstrains and residual stresses in autofrettaged spherical pressure vessels. J. Press. Vessel Technol. **139**, 041202 (2017)
23. K.K. Zur, S.A. Faghidian (eds.), *Nanomechanics of Structures and Materials Modeling and Analysis* (Elsevier, 2024)
24. S.A. Faghidian, A. Tounsi, Dynamic characteristics of mixture unified gradient elastic nanobeams. Facta Universitatis Series: Mech. Eng. **20**, 539–552 (2022)
25. A. Davlatov, G. Gulyamov, A. Nabiyev, E. Feddi, K. Feddi, A. Abdukarimov, A. Botirjonov, Unraveling the effects of nonparabolicity on electron energy levels in InP/InAs/InP heterostructures. Phys. Scr. **99**, 075933 (2024)
26. S. Adachi, *Properties of Group-IV, III–V and II–VI Semiconductors* (Wiley, New York, 2005)
27. I. Mal, J. Jayarubi, S. Das, A.S. Sharma, A. J.Peter, D.P. Samajdar, Hydrostatic pressure dependent optoelectronic properties of InGaAsN/GaAs spherical quantum dots for laser diode applications. Phys. Status Solidi (b). (2018). https://doi.org/10.1002/pssb.201800395

28. G. L. Bir, G. E. Pikus, Symmetry and Strain-Induced Effects in Semiconductors, Wiley, New York (1976)
29. A. Luque, A.V. Mellor, *Photon Absorption Models in Nanostructured Semiconductor Solar Cells and Devices* (SPIE, Bellingham, Washington, 2015)
30. Y.P. Varshni, Temperature dependence of the energy gap in semiconductors. Physica. **34**, 149–154 (1967)
31. R. Arraoui, K. El-Bakkari, K. Limame et al., Pressure and temperature influences on the nonlinear optical rectification of an impurity in a symmetrical double quantum dot. Eur. Phys. J. Plus. **138**, 292 (2023)
32. T. Brahim, A. Bouazra, M. Said, Numerical modeling of electronic and optical properties for different sizes of CdSe/ZnS quantum dots under temperature and hydrostatic pressure effects. Opt. Quant. Electron. **56**, 346 (2024)
33. A. Ed-Dahmouny, A. Sali, N. Es-Sbai et al., The impact of hydrostatic pressure and temperature on the binding energy, linear, third-order nonlinear, and total optical absorption coefficients and refractive index changes of a hydrogenic donor impurity confined in GaAs/AlxGa1 – xAs double quantum dots. Eur. Phys. J. Plus. **137**, 784 (2022)
34. I. Vurgaftman, J.R. Meyer, L.R. Ram-Mohan, Band parameters for III–V compound semiconductors and their alloys. J. Appl. Phys. **89**, 5815–5875 (2001)
35. D.F. Nelson, R.C. Miller, D.A. Kleinman, Band nonparabolicity effects in semiconductor quantum wells. Phys. Rev. B **35**, 7770–7773 (1987)
36. D.J. BenDaniel, C.B. Duke, Space-charge effects on electron tunneling. Phys. Rev. **152**, 683–692 (1966). https://doi.org/10.1103/PhysRev.152.683
37. G. Bastard, Wave mechanics applied to semiconductor heterostructures. John Wiley& Sons: New York, (1991)
38. M. Kria, M. Farkous, V. Prasad, F. Dujardin, L. M. Pérez, E. Feddi, Wetting layer and size effects on the nonlinear optical properties of semi oblate and prolate Si0.7Ge0.3/Si quantum dots. Curr. Appl. Phys. **25**, 1–11 (2021)
39. D.J. BenDaniel, C.B. Duke, Space-charge effects on electron tunneling. Phys. Rev. **152**, 683–692 (1966).
40. S. Saravanan, A.J. Peter, C.W. Lee, Phonon effects on interband optical transitions in InAs 0.8 P 0.2 /InP quantum wire. J. Luminescence. **169**, 86–92 (2016)
41. Z.H. Zhang, J.H. Yuan, K.X. Guo, The combined influence of hydrostatic pressure and temperature on Nonlinear Optical properties of GaAs/Ga0.7Al0.3As Morse Quantum Well in the Presence of an Applied magnetic field. Materials. **11**, 668 (2018)
42. N.A. Althumairi, Optical rectification and second harmonic generation in CdSe/MgSe asymmetric double quantum wells. Heliyon. **10**, e28169 (2024)
43. Z.H. Zhang, J.H. Yuan, K.X. Guo, E. Feddi, Effect of Conduction Band Nonparabolicity on the Nonlinear Optical properties in GaAs/Ga1-xAlxAs double Semi-V-shaped Quantum Wells. Materials. **12**, 78 (2019)
44. D. Makhlouf, M. Choubani, F. Saidi, H. Maaref, Modeling of the second harmonic generation in a lens-shaped InAs/GaAs quantum core/shell dot under temperature, pressure and applied electric field effects. Results Phys. **16**, 102961 (2020)
45. Z.H. Zhang, J.H. Yuan, The third-order nonlinear optical susceptibility of AlxGa1-xAs/GaAs asymmetric triple quantum wells. Eur. Phys. J. Plus. **137**, 1367 (2022)